Check for updates

Collin Ynchausti[1]
Compliant Mechanism Research,
Department of Mechanical Engineering,
Brigham Young University,
Provo, UT 84602
e-mail: collinynchausti@byu.net

Nathan Brown
Compliant Mechanism Research,
Department of Mechanical Engineering,
Brigham Young University,
Provo, UT 84602
e-mail: nathancbrown@byu.net

Spencer P. Magleby
Compliant Mechanism Research,
Department of Mechanical Engineering,
Brigham Young University,
Provo, UT 84602
e-mail: magleby@byu.edu

Anton E. Bowden
BYU Applied Biomechanics Engineering Laboratory,
Department of Mechanical Engineering,
Brigham Young University,
Provo, UT 84602
e-mail: bowden@byu.edu

Larry L. Howell
Compliant Mechanism Research,
Department of Mechanical Engineering,
Brigham Young University,
Provo, UT 84602
e-mail: lhowell@byu.edu

Deployable Euler Spiral Connectors

Deployable Euler spiral connectors (DESCs) are introduced as compliant deployable flexures that can span gaps between segments in a mechanism and then lay flat when under strain in a stowed position. This paper presents models of Euler spiral beams combined in series and parallel that can be used to design compact compliant mechanisms. Constraints on the flexure parameters of DESCs are also presented. Analytic models developed for the force-deflection behavior and stress were compared to finite element analysis and experimental data. A spinal implant and a linear ratcheting system are presented as illustrative applications of DESCs. [DOI: 10.1115/1.4052319]

Keywords: compliant mechanisms, mechanism design

Downloaded from http://www.asmedigitalcollection.asme.org/mechanismsrobotics/article-pdf/14/2/021003/6759446/jmr_14_2_021003.pdf by guest on 03 November 2024

1 Introduction

Devices and structures that can be placed in a compact state and deployed to a larger size are desirable in many applications. One major area is medical equipment, where the increase in use of minimally invasive surgeries has led to the need for implants and devices to become smaller. However, this decrease in size, specifically of an implant, can lead to greater subsidence of bone due to less interface area between the implant and the bone. In a similar fashion, it is desirable to design space systems that can be stored and transported compactly. However, they are of little use if they cannot be deployed to the needed configuration.

The fields of origami-inspired engineering design and compliant mechanisms can be beneficial in these cases. Origami-inspired engineering presents many useful solutions to common problems in engineering design, including (1) creating designs that can achieve two or more states and (2) having these two states be a very compact state and a deployed, larger state. Additionally, the use of compliant mechanisms can be beneficial to deployable devices and structures because they can go through large deflections and store strain energy within their flexible members that can be used for the actuation of the device [1]. Although flexible members under load store strain energy that can be useful for deployment, their strained shape is largely determined by loads, boundary conditions, material properties, and geometry. The typical shape used to meet these requirements is unlikely to be compact. This presents an opportunity to develop concepts for shapes that, inspired by origami design, have a more compact stowed volume. In determining a candidate shape for a flexible member that will deflect into a compact volume, an Euler spiral, a curve that exhibits a linear change of curvature along its arc length is a potential candidate. A flexible member with this shape lies flat when a force is applied at its end. A compliant segment based on the Euler spiral could connect rigid segments and enable them to stow flat.

The objective of this paper is to introduce a compliant flexure based on combinations of Euler spirals, hereafter called the deployable Euler spiral connector (DESC), which allows a device to achieve a compact, stowed state with stored strain energy that can be released for deployment.

2 Background

Origami-inspired design provides systems where mechanisms can achieve two or more desired states (e.g. stowed and deployed). This idea of multiple achievable states is one of the inspirations for the DESCs described here. Compliant mechanisms and origami design principles have allowed designers to fabricate mechanisms in-plane. Compliant mechanisms using volume efficient shapes allows volume efficient devices.

[1]Corresponding author.

This work has been expanded from work presented at the ASME 2019 International Design Engineering Technical Conferences & Computers and Information in Engineering Conference (IDETC/CIE 2019) as IDETC2019-97456.

Contributed by the Mechanisms and Robotics Committee of ASME for publication in the Journal of Mechanisms and Robotics. Manuscript received October 5, 2020; final manuscript received August 11, 2021; published online September 20, 2021. Assoc. Editor: Zhong You.

 Copyright © 2021 by ASME

2.1 Origami-Inspired, Compliant Deployable Designs. Origami-inspired design produces mechanisms that have been used to solve problems in many different areas such as packaging designs [2,3], aerospace [4] and space-application designs [5–7], structural and disaster management designs [8,9], robotics [10,11], and medical device designs [12]. In these cases, a stowed state and different deployed state of the device are desirable.

Deployable designs are desirable in many other applications, such as antennas [13] and reflectors [14], medical devices [15–20], a deployable glider [21], a ballistic barrier [22], a train fairing [23], and even an aquatic animal capturer [24]. Deployable designs can be achieved using origami patterns [25–32], shape memory polymers [33], spatial linkages [13,34–39], developable mechanisms [40], motorized joints, coils of flexible materials, inflation, telescoping pieces, pinned joints [41], and scissor-like elements [42,43], to name a few. Some deployable mechanisms rely on the use of rigid-body members, while others use compliant flexures.

Compliant mechanisms can be beneficial in these applications because they gain at least some of their motion from compliant or flexible, members [1]. These flexible members can be designed to enable a desired deflection and a desired reaction force [44–46]. Compliant mechanisms store energy within their flexures as they deform and this strain energy can be released to deploy the mechanism when the holding force is released. The strain energy can be used as a basis for actuation of the mechanisms, reducing the complexity of actuation. With the use of compliant mechanisms and ideas derived from origami, a shape that will provide a highly efficient stowed volume can be determined.

2.2 Euler Spiral. An Euler spiral is a spiral with curvature that is a linear function of the arc length (e.g., $\kappa = Cs$, where C is a constant and s is a distance along an arc-length). The shape was originally developed to solve the elastica problem posed by Bernoulli, finding the curvature of a beam that would lay flat when a weight is placed on the beam end, but has also been used to solve other problems [47]. It is also known as a "Cornu Spiral", "spiro", or "clothoid." An example of an Euler spiral is shown in Fig. 1. The general equations for the x and y locations of a point on the spiral, as shown in Ref. [48], are given by

$$x = \int_0^a \cos(\theta(s))\,ds = C\int_0^a \cos(s^2)\,ds$$
$$y = \int_0^a \sin(\theta(s))\,ds = C\int_0^a \sin(s^2)\,ds \quad (1)$$

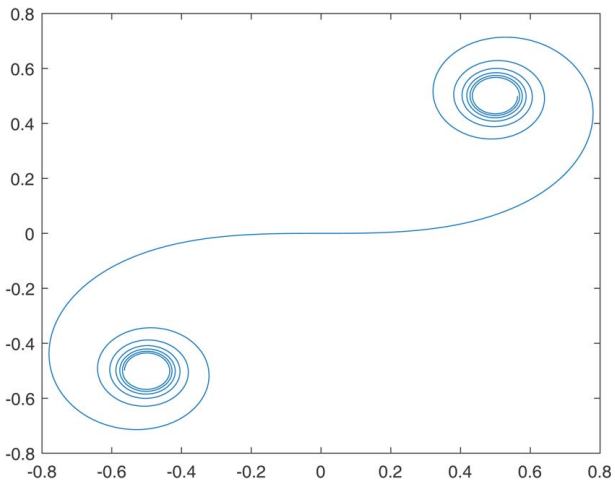

Fig. 1 Euler Spiral plotted using $B = C(\alpha) + iS(\alpha)$, where $C(\alpha)$ and $S(\alpha)$ are Fresnel integrals, and α has a range of −5 to 5

where C is a proportionality constant, a is the distance along the arc-length that the x and y position is desired, and $\theta(s)$ is the beam angle as a function of s, which in the case of an Euler spiral is Cs^2.

Because the curvature of the spiral is a linear function of the arc length, the curve creates a smooth, gradual transition. This characteristic has been beneficial in modeling intersection dynamics [49], designing roads and railroad tracks [50], and performing curve-completion in graphics applications [51,52]. Yellowhorse and Howell [48] used the Euler spiral to model and design lenticular stiffeners that provide additional stiffness to deployable space arrays where the stiffener would lay flat when stowed. The concept of the Euler spiral was used to create a device that when stowed takes the least amount of space. The resulting equations are employed, extended, and validated in this paper to create the DESC design.

The work in Ref. [48] can be leveraged to provide a starting place for the fundamental equations used here. Significant differences include geometry (DESCs are antisymmetric combinations of Euler spirals), motion (the lenticular stiffeners require sliding motion between adjacent panels), boundary conditions (DESCs are connected to both parallel panels), and system intent and corresponding performance metrics (lenticular stiffeners are meant to increase system stiffness while DESCs provide a means to guide an efficient deployment system).

The rest of the paper is organized as follows. In Sec. 3, DESC design is shown with the governing constraint equations. The analytical force-deflection equation is also presented. Finite element analysis (Sec. 4) and experimental data (Sec. 5) are presented to validate the design equations presented. Section 5.3 presents a discussion on the agreement of the analytical solutions with the FEA and experimental data. In Sec. 6, two applications are presented where the use of DESCs is beneficial. Section 7 presents the conclusions of this new flexure design.

3 Deployable Euler Spiral Connectors

The proposed Deployable Euler Spiral Connector (DESC) can be combined to connect two rigid bodies, as shown in Fig. 2. The DESCs allow the device to move from a deployed to stowed configuration. The DESCs span the distance between the deployed and stowed states, such that the flexible segments act as connections between rigid segments and space filler when the structure is deployed. When the mechanism is being stowed, the connections act as guiding mechanisms.

The connectors are manufactured in or past their deployed state, so their low energy state occurs when deployed. When the connectors are stowed, the energy input to stow them is transformed into strain energy in the connectors. When the stow force is released,

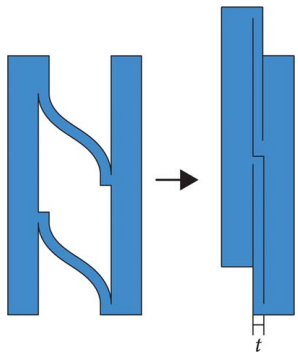

Fig. 2 Two parallel DESCs are shown connecting two rigid segments of a device. Both the deployed (left) and stowed (right) configurations are shown. The compliant members lay flat in the stowed configuration, resulting in an efficient stowed volume.

Downloaded from http://www.asmedigitalcollection.asme.org/mechanismsrobotics/article-pdf/14/2/021003/6759446/jmr_14_2_021003.pdf by guest on 03 November 2024

the strain energy is released to move the connectors to their deployed, low energy, state.

To explain the behavior of the DESC flexures, the mechanical behavior of simpler connector geometries will first be examined. Straight connectors would be the simplest connection type, as shown in Fig. 3. For the straight connections to bridge a gap, they need to be connected between the rigid members at angles between 0 and $\pi/2$ radians. When a device with these connectors is stowed, the connectors bend and a part of them contacts the rigid members, therefore, the device is not totally flat (see Fig. 3).

If the connector shape used was only the shape of a single Euler spiral, one end of the connection would not align parallel with the rigid member, as shown in Fig. 4, and the rigid members would not lay flat. Therefore, the DESC shape is antisymmetric Euler spirals connected at their points of zero curvature, as shown in Fig. 2. If the flexible segment is a DESC, it can be aligned with both ends parallel to the rigid members.

3.1 Geometry Definition. The Euler spiral equations used in Ref. [48] were modified to define the desired antisymmetric geometry. The segment should have an initial curvature, κ_0, at $s = 0$, zero curvature at $s = L/2$, and curvature, $-\kappa_0$, at $s = L$. Applying these conditions with the fact that the curvature is a linear function of arc length, the curvature, κ, is defined as

$$\kappa(s) = \mu\left(\frac{L}{2} - s\right) \tag{2}$$

where the proportionality constant, μ, is

$$\mu = \frac{2\kappa_0}{L} \tag{3}$$

where κ_0 is the initial (and maximum) curvature, s is the arc length between the origin and desired position on the curve, and L is the total arc length of the curve. The beam angle along the arc length, $\theta(s)$, is

$$\theta(s) = \frac{\kappa_0}{L}(Ls - s^2) \tag{4}$$

Using the Taylor Series approximations for the sine and cosine in Eq. (1) and substituting Eq. (4) provides the equations to define the antisymmetric geometry as

$$\frac{x(s)}{L} = \frac{1}{L}\int_0^s \left(1 - \frac{\theta(s)^2}{2}\right) ds \approx -\frac{p^5q^2}{10} + \frac{p^4q^2}{4} - \frac{p^3q^2}{6} + p \tag{5}$$

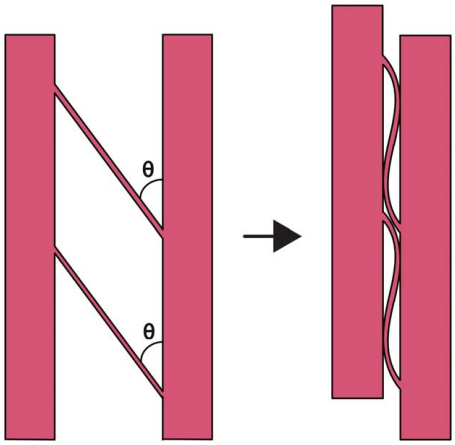

Fig. 3 Two parallel straight connections are shown connecting two rigid segments of a device. Both the deployed (left) and stowed (right) configurations are shown. The compliant members do not lay flat in the stowed configuration, resulting in an ineffective use of space and higher stresses.

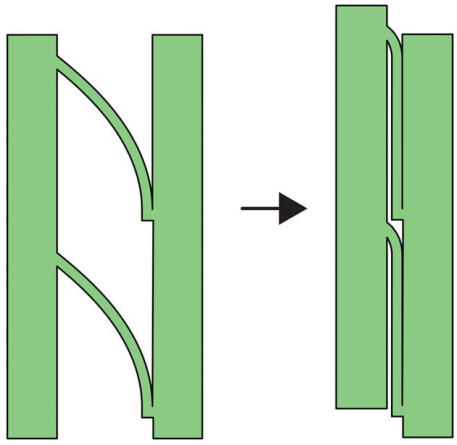

Fig. 4 Mechanism using an Euler Spiral connection. The left side of this connection will not allow the mechanism to lay flat when stowed due to the attachment to the rigid body. If one end is not attached and allowed to slide, it results in friction.

and

$$\frac{y(s)}{L} = \frac{1}{L}\int_0^s \left(\theta(s) - \frac{\theta(s)^3}{6}\right) ds \approx \frac{p^7q^3}{42} - \frac{p^6q^3}{12} + \frac{p^5q^3}{10} - \frac{p^4q^3}{24} - \frac{p^3q}{3} + \frac{p^2q}{2} \tag{6}$$

where

$$p = \frac{s}{L} \tag{7}$$

and

$$q = \kappa_0 L \tag{8}$$

These connections should span a desired distance in the x- and y-directions, so the final x- and y-coordinates are known, when $s = L$, then $x(s) = x(L) = x_{\text{final}}$, and $y(s) = y(L) = y_{\text{final}}$. At $s = L$, $p = 1$ and Eqs. (5) and (6) can be simplified to

$$\frac{x(L)}{L} = -\frac{q^2}{10} + \frac{q^2}{4} - \frac{q^2}{6} + 1 = -\frac{q^2}{60} + 1 \tag{9}$$

and

$$\frac{y(L)}{L} = \frac{q^3}{42} - \frac{q^3}{12} + \frac{q^3}{10} - \frac{q^3}{24} - \frac{q}{3} + \frac{q}{2} = -\frac{q^3}{840} + \frac{q}{6} = -\frac{q}{6}\left(\frac{q^2}{140} - 1\right) \tag{10}$$

Equations (9) and (10) have four unknowns or design inputs: L, κ_0, x, and y. With the equations, two of the four design inputs need to be chosen to solve for the other two unknowns.

3.2 Design Parameters and Limitations of DESCs. The following sections define behaviors and mechanical limitations to take into account when designing DESCs.

3.2.1 Force to Stow. The force per unit width needed to fully flatten a lenticular stiffener is $\overline{F} = \kappa_0 E t^3/12L_{ls}$ [48], where E is the modulus of elasticity of the material, t is the in-plane thickness of the connector (see Fig. 5), and L_{ls} is the arc length of the lenticular stiffener in Ref. [48].

Downloaded from http://www.asmedigitalcollection.asme.org/mechanismsrobotics/article-pdf/14/2/021003/6759446/jmr_14_2_021003.pdf by guest on 03 November 2024

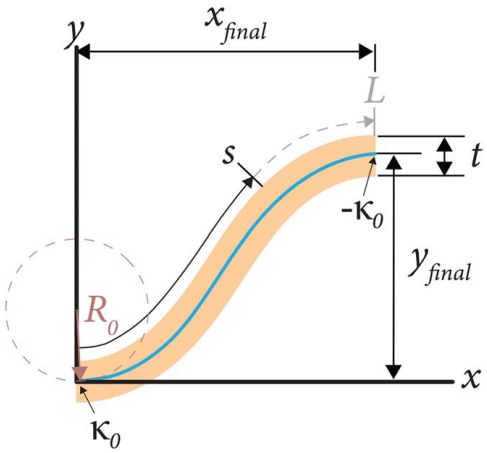

Fig. 5 The key parameters for determining the equations of the DESC. The distance along the arc length is defined as *s* and can vary from 0 to *L*, where *L* is the total arc length of the flexure. x_{final} is the horizontal distance of the undeflected flexure, and y_{final} is the vertical distance of the undeflected flexure. These distances represented the desired distances for the flexure to span. The initial (and maximum) curvature, κ_0 is also shown along with the circle of radius R_0 that defines the initial curvature ($\kappa_0 = 1/R_0$). The solid line represents the spiral. The shaded region represents the offset of the spiral in both directions to account for material thickness.

For a DESC of length L, composed of two spiral sections of length $L/2$, the DESC could be modeled as two springs in series, the force per unit width to compress the entire DESC is equal to the force per unit width to compress half the segment. Thus, the force per unit width to fully compress a DESC flexure is

$$\overline{F}_{\text{DESC}} = \frac{\kappa_0 E t^3}{6L} \tag{11}$$

Using Eq. (11) and defining the number of DESC flexures in parallel as n gives the total force as

$$\overline{F}_{\text{total}} = n\frac{\kappa_0 E t^3}{6L} \tag{12}$$

For designs where there are DESC flexures in parallel and in series, Eq. (12) is modified to become

$$\overline{F}_{\text{total}} = \frac{2n_1 n_2}{n_1 + n_2}\frac{\kappa_0 E t^3}{6L} \tag{13}$$

where n_1 is the number of DESCs in parallel in the top row and n_2 is the number of DESCs in parallel in the bottom row, as shown in Fig. 6.

3.2.2 Force-Deflection Curve: Boundary Value Problem (BVP). The curvature of a thin elastic beam is

$$\kappa = \frac{d\theta}{ds} = \frac{M}{EI} + \kappa_i \tag{14}$$

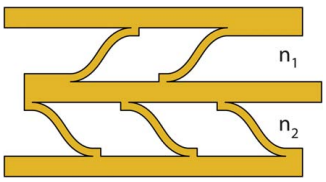

Fig. 6 A mechanism with DESCs in parallel and series. The top row has 2 (n_1) DESCs and the bottom row has 3 (n_2) DESCs in parallel.

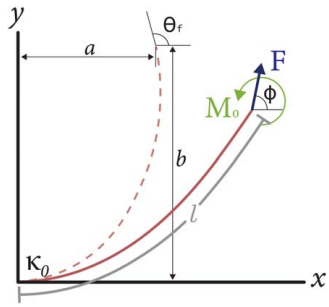

Fig. 7 Half DESC (Euler Spiral) model used in the derivation of the force-deflection curve. *L* is the arc length of the beam, κ_0 is the initial curvature of the beam, ϕ is the angle from the positive *x*-axis of the applied force, θ_f is the end point angle of the deflected beam, *F* is the applied force, M_0 is the applied moment, and *a* and *b* are the horizontal distance from the *y*-axis and the vertical distance from the *x*-axis to the beam end point, respectively.

where κ_i is the initial curvature of the beam, M is the moment on the beam, I is the area moment inertia of the beam, and E is as described earlier.

The beam shown in Fig. 7 has a moment load, M_0, and a force load, F, applied at an arbitrary angle, ϕ. Arbitrarily cutting a segment of the beam and taking the moment, M, at the cut point yields

$$M = M_0 + F\sin\phi(a - x) - F\cos\phi(b - y) \tag{15}$$

Substituting Eq. (15) for the moment, M and $\kappa_i = (\kappa_0/l)(l - s)$ into Eq. (14) gives the curvature as

$$\frac{d\theta}{ds} = \frac{F}{EI}\left[\sin\phi(a - x) - \cos\phi(b - y)\right] + \frac{M_0}{EI} + \frac{\kappa_0}{l}(l - s) \tag{16}$$

Differentiating Eq. (16) with respect to s yields

$$\frac{d^2\theta}{ds^2} = \frac{F}{EI}\left(-\sin\phi\frac{dx}{ds} + \cos\phi\frac{dy}{ds}\right) - \frac{\kappa_0}{l} \tag{17}$$

Substituting the identities $dx/ds = \cos\theta$ and $dy/ds = \sin\theta$ into the equation, and simplifying, produces

$$\frac{d^2\theta}{ds^2} = \frac{F}{EI}\sin(\theta - \phi) - \frac{\kappa_0}{l} \tag{18}$$

with boundary conditions at the beam end of

$$\theta(0) = 0$$
$$\theta'(l) = \frac{M_0}{EI} \tag{19}$$

Equation (18) can be solved using numerical integration methods and the beam endpoints, (a, b), can be determined for any given M_0, F, and ϕ.

Specifically in the case of the half DESC, in Fig. 7, a force is applied on the flexure in the negative y-direction ($\phi = 3\pi/2$ radians), and no moment is applied to the flexure ($M_0 = 0$), producing $\theta'(l) = 0$ for the second boundary condition in Eq. (19). Due to the symmetric nature of the DESC (the DESC being the two antisymmetric half Euler Spirals), the displacements due to the force determined in the solution to Eq. (18) can be doubled because the flexure acts as two springs in series. This provides the force-deflection relationships of the DESC.

3.2.3 Avoiding Over Stress—The Elastic Strain Limit. The maximum stress is $\sigma_{\max} = M_{\max} t/2I$, where $M_{\max}$ is the maximum moment in the beam and I is the area moment of inertia of the

Downloaded from http://www.asmedigitalcollection.asme.org/mechanismsrobotics/article-pdf/14/2/021003/6759446/jmr_14_2_021003.pdf by guest on 03 November 2024

beam. According to the Euler–Bernoulli beam theory for thin elastic beams, $\kappa = M/EI$, where κ and M are the curvature and moment, respectively, at a specific distance on the beam.

The initial curvature, κ_0, is the maximum curvature of the DESC, therefore $\kappa_0 = M_{max}/EI$. Rearranging this equation to solve for the maximum moment in terms of the curvature and substituting into the stress equation, the maximum stress, σ_{max}, for a DESC flexure results in

$$\sigma_{max} = \frac{\kappa_0 E t}{2} \tag{20}$$

which is consistent with the results for lenticular stiffeners in Ref. [48]. Because the maximum curvature is located at the connections to the rigid segments, the maximum stress will occur at these locations.

As can be seen in Eq. (20), the stress is dependent on the material properties of the flexure, and the maximum curvature and thickness of the flexure. Having a non-dimensional parameter that provides a limit for what values the maximum curvature and thickness of the flexure can be without yielding due to stress would be a useful parameter to aid in the design of these flexures. Incorporating a safety factor, n, to the maximum stress in Eq. (20) and equating this value to the yield strength, S_y, the non-dimensionalized product of the curvature and thickness, the elastic strain value ($\kappa_0 t$), can be solved for

$$\kappa_0 t \leq \frac{2}{n}\left(\frac{S_y}{E}\right) \tag{21}$$

This provides a straightforward parameter limit, defined here as the "elastic strain limit," that is particularly useful in designing DESCs that maintain stress below the yield strength. Equation (21) also illustrates that another important parameter for the curvature of the DESCs is the yield strength to Young's modulus ratio, S_y/E. If this ratio is high, higher initial curvatures to a constant flexure thickness are possible without plastic deformation of the flexure during the stowing motion.

3.2.4 Avoiding Overcurvature—The Critical Curvature Constant. Because the flexure's curvature is linearly proportional to the arc length of the flexure, the value of proportionality determines in what increments this linear change occurs. Equations (3) and (4) show the linear change is dependent on κ_0/L. This means that depending on the length of L, the increment at which the curvature changes may be smaller or larger. When L is smaller, then the proportionality is large and the change in curvature and angle along the beam has a larger change per unit length, while if L was larger, the inverse occurs. If L becomes too large compared to κ_0, the flexure can become overcurved. A flexure is overcurved if the slope (θ) at the midpoint of the flexure is greater than $\pi/2$. A flexure whose angle at the midpoint is equal to $\pi/2$ is defined as critically curved. A flexure where the slope at the midpoint is less than $\pi/2$ is undercurved and desirable. In all these cases, the flexure is the shape of an Euler Spiral; however, an overcurved flexure will not lie flat when a vertical force is applied but will lie on itself, nullifying the purpose of the flexure (Fig. 8).

The "critical curvature constant" is defined as the value where overcurvature begins to occur. Unlike the "elastic strain limit," this value is only dependent on the geometry of the flexure. To avoid overcurvature, the beam angle, $\theta(s)$, at the midpoint of the flexure ($s = L/2$) needs to be less than or equal to vertical ($\theta(L/2) \leq \pi/2$). Substituting these values into Eq. (4) and solving for the non-dimensional product of the curvature and length, the equivalent curvature ($\kappa_0 L$) yields

$$\kappa_0 L \leq 2\pi \tag{22}$$

Because an approximation was used to define the DESC flexure, another value of the critical curvature constant needs to be determined. Similar to the process above, the x portion of the parametric function (Eq. (5)) was differentiated with respect to s to determine the equation of the beam angle. Then, imposing the constraint that the change in x with respect to s needs to be greater than zero when $s = L/2$ ($dx/ds_{s=L/2} \geq 0$) produces

$$\kappa_0 L \leq 4\sqrt{2} \approx 5.66 \tag{23}$$

With flexures that are critically curved or not extremely overcurved, the deflection of the flexure may or may not follow the normal DESC motion and lay flat upon an applied vertical load. Equation (23) helps to determine the limits to which flexures can be used without voiding the ability to lay flat.

3.3 Error of Taylor Series Approximations. The error of the spiral geometry due to the Taylor series approximation was determined by comparing the $x(s)/L$ and $y(s)/L$ values for the analytical solution and Taylor Series approximation for $p = 0 \rightarrow 1$ and $q = 0 \rightarrow 2\pi$, as this is the limiting factor for a DESC as shown in Sec. 3.2.4. The error is the distance between the exact and approximate points, calculated by

$$\text{error} = \sqrt{\left[\left(\frac{x(s)}{L}\right) - \left(\frac{x(s)}{L}\right)_{\text{Taylor}}\right]^2 + \left[\left(\frac{y(s)}{L}\right) - \left(\frac{y(s)}{L}\right)_{\text{Taylor}}\right]^2} \tag{24}$$

Figure 9 shows the error for the above values of p and q. The maximum error using the Taylor Series approximations with q equal to 2π does not exceed 10%.

3.4 Other Observations. The case of the three DESCs in parallel provides a statically indeterminate situation. However, because the flexures are much thinner than the rigid members, the DESCs can be assumed to be the only piece of the device that is deflecting. And, because the flexures lying flat is the main concern, the third DESC only contributes to an increase of the force needed to stow the device, as shown in Eqs. (12) and (13).

Because the motion of mechanisms using DESCs is dependent on the deflection of beams, considerations must also be taken during design to account for the amount of energy that will be stored within the flexure. While this energy is needed to stow the device, the benefit of using a compliant flexure is that a device with DESCs can be used to store strain energy. This stored strain energy can provide actuation for the device to move to the deployed state. This stored strain energy can also be used to provide a compact biasing force to increase precision in assemblies with clearances or can act as an ultra compact spring in mechanical systems where space is at a premium.

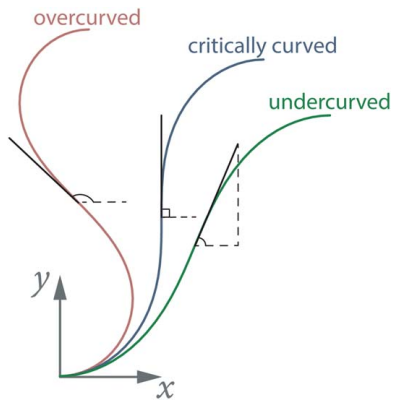

Fig. 8 Different variations of curvature of a DESC. All three curves have the same maximum curvature, κ_0, with differing lengths, L.

Downloaded from http://www.asmedigitalcollection.asme.org/mechanismsrobotics/article-pdf/14/2/021003/6759446/jmr_14_2_021003.pdf by guest on 03 November 2024

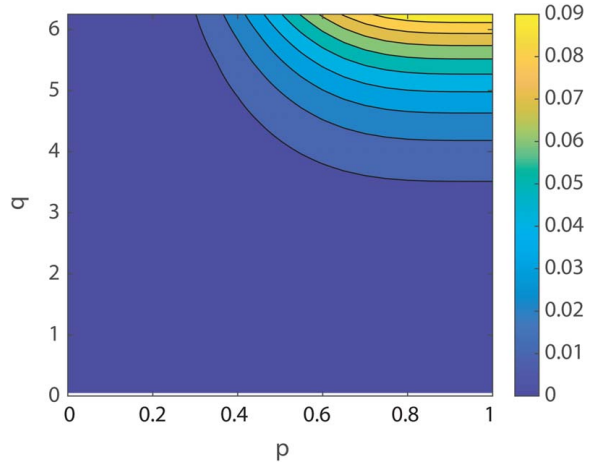

Fig. 9 Plot showing the error determined by $y/L - (y/L)_{Taylor}$. The maximum error does not exceed 10%.

Table 1 Flexural moduli as determined from a three-point bend test

Thickness (mm)	Flexural modulus of elasticity (MPa)
1	114
2	103
3.2	123

In many cases, the number of cycles a DESC flexure will experience will be low because it is used for deployment; however, other cases may have higher cycles and a more detailed fatigue analysis. In these cases, Eq. (20) can be used with appropriate fatigue failure theories to determine the limiting values of the flexure parameters to avoid fatigue failure.

4 Comparison to Finite Element Analysis

DESC flexures were modeled in finite element analysis (FEA) software to evaluate the analytical models presented earlier. The flexural moduli were determined from the three-point bend tests discussed in Sec. 5.1 and are listed in Table 1. With the moduli in this table, the theoretical force to fully stow each DESC, the force-deflection curve, and maximum stress in the flexure was determined using Eqs. (12), (18), and (20), respectively, and FEA was performed.

4.1 Finite Element Analysis Comparison. Finite element analysis (FEA) was performed, using ANSYS MECHANICAL APDL, on a curve defining the spiral flexure with the parameters as shown in Table 2. The curve was meshed using BEAM188 elements. The section was split into 10×10 elements with each element being 0.1 mm long. All degrees-of-freedom (DOF) were constrained at the base of the flexure. The in-plane rotation of the top end of the flexure was constrained to zero, and the y-displacement was set to -11.5 mm. Geometric nonlinearities were also included in the analysis. The reaction force and the Von Mises stress in the flexure were determined and are shown in Table 2. The flexure deflection and Von Mises stress distribution are shown in Fig. 10. As expected, the flexure lies essentially flat and the maximum stress occurs at the top and bottom of the flexure at its ends.

FEA was also performed on curves of different parameters, shown in Table 2, using the same meshing parameters as described earlier. The results of these studies are also presented in Table 2.

To evaluate the accuracy of the presented models, the values of the force to stow, maximum stress, and maximum deflection of the DESCs were used to calculate the differences. The percent differences for the force to stow were calculated with the FEA value. The percent difference for the maximum stress was calculated with the FEA value being considered the true value. Because the force deflection curve was determined using the maximum force calculated from Eq. (12), the difference in deflection was used to determine how accurate the models were. The value found using Eq. (18) was used as the true value in this case.

4.2 Finite Element Analysis Results. Table 2 shows the results of the models and FEA along with the comparisons of agreement between models and FEA. The percent difference between the models and the FEA is no greater than 5.5% in any of the cases for the force to stow, maximum stress, and the maximum deflection of the DESC. These results show that Eqs. (12), (18), and (20) provide reasonable predictions of the DESC behavior.

5 Comparison to Experiment

Physical testing of hardware was performed and compared to the analytical equations and FEA presented in this work to further discover the accuracy of the models. A three-point bend test was used to approximate the flexural modulus of elasticity of the material. DESC prototypes were also made and tested to determine the maximum stow force. Testing was performed on an Instron 3345 tensile tester with a position control resolution of 0.133 μm.

5.1 Experimental Test Procedure. *Three-Point Bend Test.* Flat rectangular bars of 1.0, 2.0, and 3.2 mm thicknesses were 3D printed in Polyflex (TPU95) to be used in a three-point bending test to determine the flexural modulus of elasticity of Polyflex. Ten samples of each thickness were manufactured and tested.

Table 2 Values obtained using analytical equations and FEA for different DESC configurations

		$\kappa_0 = 0.19$ rad/mm		$\kappa_0 = 0.39$ rad/mm	
		$L = 19.9$ mm		$L = 12.8$ mm	
Configuration		$t = 1$ mm	$t = 2$ mm	$t = 1$ mm	$t = 2$ mm
Force to stow (N/mm)	Eq. (12)	0.18	1.32	0.58	4.17
	FEA	0.19	1.33	0.61	4.2
	Percent difference (%)	5.3	0.8	4.9	0.7
Maximum stress (MPa)	Eq. (20)	10.83	19.64	22.22	40.31
	FEA	11.10	19.60	22.8	38.70
	Percent difference (%)	2.5	0.2	2.5	5.5
Maximum deflection (mm)	Y-distance of flexure	11.50		8.76	
	Eq. (18)	11.31		8.87	
	Percent difference (%)	1.7		1.2	

Downloaded from http://www.asmedigitalcollection.asme.org/mechanismsrobotics/article-pdf/14/2/021003/6759446/jmr_14_2_021003.pdf by guest on 03 November 2024

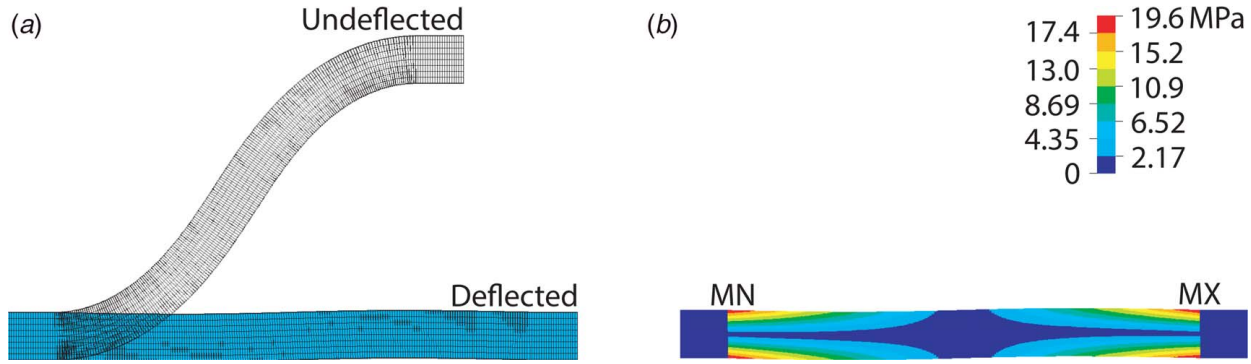

Fig. 10 The deflection of and the stress in the 2-mm-thick DESC with initial curvature of 0.19 rad/mm: (*a*) undeflected and deflected shape and (*b*) the Von Mises stress distribution in the DESC. As expected, the maximum stress occurs at the flexure connections where the change in curvature is maximum.

The rectangular Polyflex bars were 3D printed with the thickness (y-direction) and length (x-direction) in the plane of the printer. The width of the bars was printed in the z-direction to match the direction in which the DESC flexures were printed.

The three-point bend test setup, consisting of a base and plunger were made according to dimensions listed in the ASTM D790 standard [53]. Three different-sized stationary bases were used with the three corresponding sample thicknesses. With the stationary base secured to the bottom of the fixture, the plunger was attached to the load cell and then mounted onto the cross head. For the 2 and 3.2 mm samples, the system was setup to measure the data using an Interface SMT1-22 98 N load cell with an uncertainty of 0.03%. For the 1 mm samples, the system was setup to measure the data using an Interface SMT1-1.1 5 N load cell with an uncertainty of 0.04%. After setup, the load cell was calibrated, and the displacement zeroed.

Each sample set was tested according to ASTM D790 [53], and the load-displacement data was recorded. The force was zeroed between samples to ensure that the recorded force reflects the force due to the added displacement in each individual sample.

After testing, a statistical analysis was performed on the collected data, and a model was fit to the data. All variables were considered with their interactions to create possible models to fit the data using multiple linear regression models. The minimum Bayesian information criterion (BIC) was used to determine the best model for each sample set. Case-Influence statistics such as Cook's distance, leverage, and studentized residuals were calculated to ensure that no data was seriously affecting the models. Once the models were created, the modulus of elasticity for each case was calculated using Eq. (6) in the ASTM D790-17 standard [53].

Compression Testing to Determine Maximum Stow Force. Testing of DESC prototypes was performed using the test setup shown in Fig. 11. DESCs of different curvatures, lengths, and thicknesses were tested. Combinations of the tested DESCs are shown in Table 2. For each curvature-length-thickness combination, three samples were printed.

Test samples were made of 4 DESCs with two parallel DESCs in series with two other parallel DESCs, as shown in Fig. 11. Each sample was printed as a single piece. This configuration leads to measured forces of two times the forces needed to displace one DESC. This mechanism setup (four DESCs) was chosen because it allowed the DESCs to be deflected in a guided motion and the bottom surface did not slide relative to the top surface.

To get an accurate force reading (without seeing a force spike due to contact), each test specimen was deflected 95% of its total deflection distance. The force at this value was taken as the maximum force. An Interface SMT1-22 98 N load cell with an uncertainty of 0.03% was used to test the DESC samples. The load cell was calibrated after setup, before performing testing, and was zeroed between samples.

Each of the samples were tested in order, being compressed to 95% of the total displacement. After being tested, the samples were allowed to "relax" back to their original positions. The samples were then retested using this procedure 10 times each. Testing the three samples in order allowed at least 2 min of relaxation time for each sample before being re-tested.

A statistical analysis was performed on the measurement data collected. All variables were considered with their interactions to create possible models to fit the data using multiple linear regression models. The minimum BIC criteria were again used to determine the best model for each sample set. Case-Influence statistics such as Cook's distance, leverage, and studentized residuals were again calculated to ensure that no data was seriously affecting the models. A 95% individual confidence interval was also calculated for the fit.

5.2 Experimental Results. The mean experimental force per unit width model curve for the 0.19 rad/mm, 19.9 mm long, 1 mm thick DESC flexure shown in Fig. 12. The calculated value found from Eq. (12) was also used as the maximum force per unit width value in the boundary value problem (BVP) to determine the force-deflection curve using Eq. (18). Both these values are also shown in Fig. 12 along with the FEA data. As a note, in this calculation, the full equation of an Euler spiral was used instead of the Taylor Series approximations.

An array with two parallel DESCs on the top row and three parallel DESCs on the bottom row was also tested to verify Eq. (13). The force to stow this array was calculated to be 37 N. This configuration was also measured to have a maximum force of 35 N. This yields a percent difference of approximately 6.8% between calculated and measured forces.

5.3 Comparison of Results. Figure 12 shows the experimental results for the 0.19 rad/mm, 19.9 mm long, 1 mm thick DESC flexure. The results follow the same trend lines as do the force-deflection curves developed using Eq. (18) and FEA, although it can be seen that near the end the analytical and experimental trend lines deviate. One source of the difference is that the material properties of the test specimens were approximated to be linear when TPU95 exhibits nonlinear material properties. Although the deviation is slight in the first three configuration cases (0.19 rad/mm, 19.9 mm long, 1 mm thick; 0.19 rad/mm, 19.9 mm long, 2 mm thick; 0.39 rad/mm, 12.8 mm long, 1 mm thick), the experimental results deviate highly from the analytical line for the fourth configuration (0.39 rad/mm, 12.8 mm long, 2 mm thick). This sharp curvature and higher thickness results in strains that cause the nonlinear properties of TPU95 to be exhibited, including localized yielding of the flexures on the outer portions of the flexures due to exceeding the material tensile strength.

Downloaded from http://www.asmedigitalcollection.asme.org/mechanismsrobotics/article-pdf/14/2/021003/6759446/jmr_14_2_021003.pdf by guest on 03 November 2024

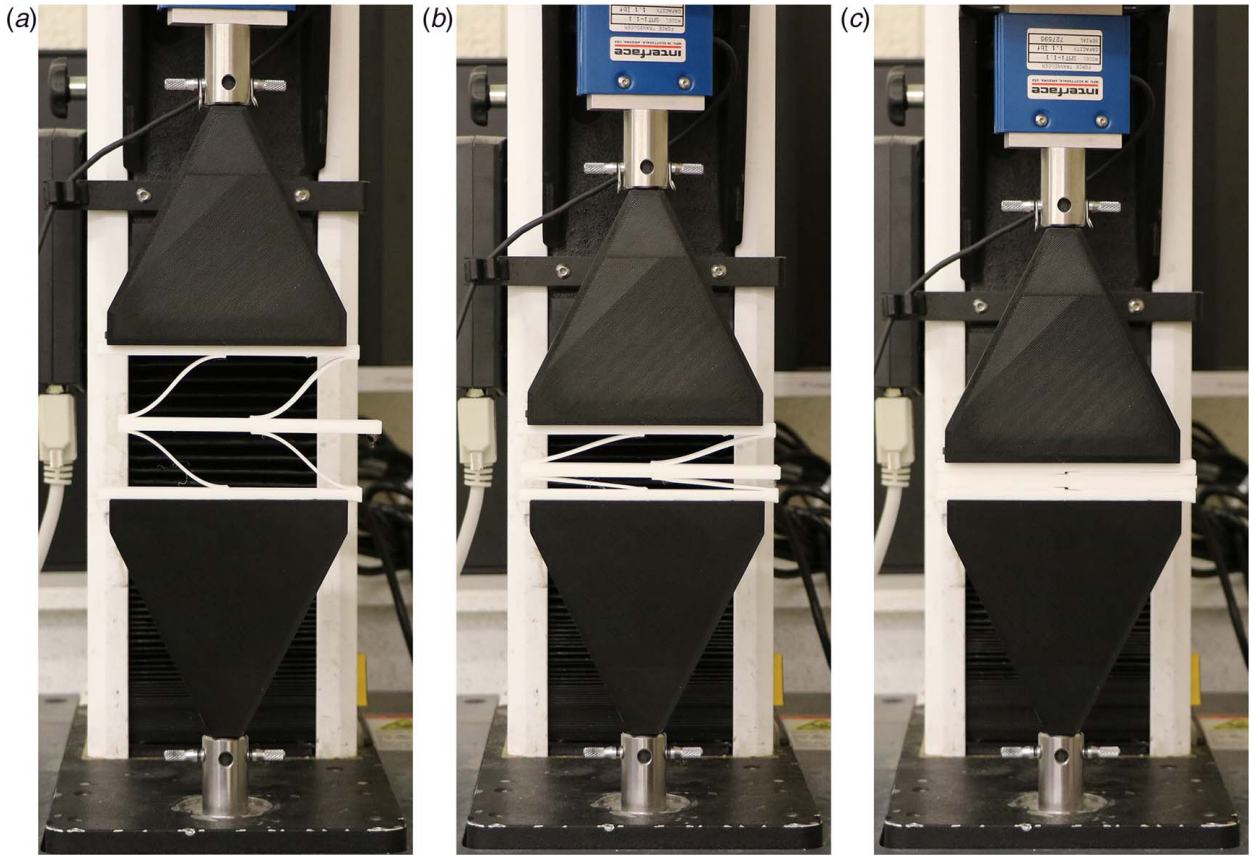

Fig. 11 Experimental setup and compression testing of the DESCs: (*a*) experimental test setup with DESC fully expanded, (*b*) compression test with the DESC partially compressed, and (c) compression test with the DESC fully compressed

Other factors may have also contributed to the deviation. Possible effects include the unmodeled effects of gravity (which have a larger effect for more flexible designs), unequal compression of the different levels, the effects of layers from 3D printing the samples (including delamination of layers, which was observed in at least one sample), manufacturing imperfections due to limitations of the 3D printing process used, and the flexibility of the end connections that were modeled as rigid.

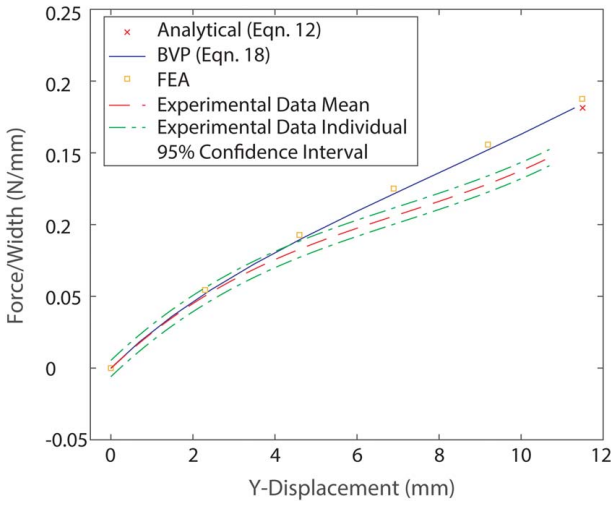

Fig. 12 Force deflection curve for the DESC with initial curvature of 0.19 rad/mm, length of 19.9 mm, and thickness of 1 mm. The experimental curve follows the same trend as the analytical models presented but with a slight linear deviation, attributed mostly to the nonlinear material properties and the manufacturing imperfections of the 3D-printed material

The effects of manufacturing imperfections could have reduced the expected stow force, as evidenced in Fig. 11. The bottom set of DESCs compresses fully before the top set. From our assumption that these act as identical springs in series, the top set should compress at the same rate as the bottom set.

While there is some deviation for areas of higher strain, Fig. 12 shows that the motion predicted by the analytical equations and the FEA agree and that the experimental data shows the same trend of motion, with a deviation primarily due to nonlinear material properties.

The difference between the deflections presented for the two analytic solutions is mostly due to the use of the Taylor Series approximation equations to create the spiral in CAD, while the actual equation was used in Eq. (18). Even with this difference in methods, the percent difference is still under 2% for both cases.

6 Example Applications

Two applications were selected to demonstrate the application of DESCs: a spinal fusion implant and a ratchet and pawl mechanism. To understand the full benefit of DESCs to the spinal fusion implant, some background on spinal fusion surgical procedures needs to be discussed.

6.1 Spinal Fusion Background. Spinal fusion implants are a promising design application of DESCs and preliminary designs will be used here to demonstrate their potential use. The efficient stowing and deployment of the flexure can benefit a minimally invasive spinal fusion procedure.

Spinal fusion is a common procedure in the United States with about 460,000 occurring in 2014 [54]. Spinal fusion surgery is

Downloaded from http://www.asmedigitalcollection.asme.org/mechanismsrobotics/article-pdf/14/2/021003/6759446/jmr_14_2_021003.pdf by guest on 03 November 2024

performed for a multitude of different disorders [55]. During many spinal fusions, the intervertebral disc is removed. Spinal disc implants are used to maintain the disc height and stabilize the spinal column while bone fusion occurs [56]. In addition to maintaining disc height and providing stabilization, the implant will also ideally provide paths for bone to grow through and fuse together.

Different types of disc implants are used depending on the need and surgical approach technique determined to perform the spinal fusion [56,57]. Each implant has a specific profile and design that can be implanted using a specific surgical approach with a specific operative size window to perform its needed function [56]. For example, during a posterior lumbar interbody fusion, two devices are placed into the disc space that have smaller cross sections, instead of only one device as in anterior, lateral, and transforaminal fusions [56]. Each of these approaches provides a solution to maintaining disc height and providing stabilization. A larger implant area can result in a larger region of spinal load transfer (e.g., more stability and lower stress), but achieving this usually means a larger implant (and larger incision), or multiple smaller implants [56].

Because incisions are required to access the spine during fusion surgeries, the size of the incision affects the amount of area that can become infected [58] and affects the time that is required for the incision to heal. The size of the incision is partially determined by the size of equipment (i.e., smaller equipment allows for smaller incisions). While it is desired to have the smallest possible spinal devices to enable the smallest possible incisions, small fusion devices can also lead to subsidence. Subsidence is the sinking of the implant into the surrounding bone due to the differences in mechanical stiffness of the implant in comparison with the supporting bone (i.e., stress overload of the bone). The amount of subsidence ($H_{subsidence}$) that an implant will have is proportional to the forces applied to the implant (F), the difference of the moduli of the implant and the bone (E_1, E_2) and inversely proportional to the area of the interface between the implant and the bone ($A_{interface}$) [59].

Compliant mechanisms have been used in spinal implants to mimic the natural motion and stiffness of the spine [60,61]. A deployable implant could help address the seemingly contradictory requirements of a small incision and a large implant that provides stability and reduces subsidence.

6.2 Spine Fusion Implant Design. Table 3 lists the values determined in the design of the spinal fusion devices. The initial curvatures (κ_0) and lengths (L) were determined from a desired span of the flexures (x and y) and solving Eqs. (4) and (5). Many of the parameter definitions are shown in Figs. 5 and 13.

The compliant spinal device consists of five rigid members connected with DESCs, printed as a single piece. The device employs retractor wires connected to the outermost rigid segments to enable the device to be stowed and released for a controlled deployment. They also allow for the device to be retracted, in the case that the device needs to be moved during placement. The retractor lines are controlled by a rod with a screw head, tight fit into the middle rigid member. The screw head allows a screwdriver to wind and unwind the retractor wire. The tight fit causes friction between the rod and the rigid segment enabling intermediate stow positions, where the device is neither completely deployed or stowed. This feature allows for the device to be placed with some pre-strain in the DESCs to increase its stiffness. Holes are placed within the rigid segments of the disc implant to allow for bone growth through the device as part of the spinal fusion.

Table 3 Input parameters of the DESC spinal devices

Configuration	Circular	Oval	Units
Input parameters			
Circle diameter (d)	92	–	mm
Oval width (w)	–	62	mm
Oval height (h)	–	43	mm
Avg rigid segment width (b)	7.58	4.57	mm
Depth of device (d)	8	17.37	mm
Thickness of DESCs (t)	2	1.03	mm
Initial curvature (κ_0)	0.19	0.39	mm^{-1}
Arc length of DESCs (L)	19.9	12.8	mm
Horizontal span (x)	11.5	8.65	mm
Vertical span (y)	15	7.61	mm
Number of DESCs in row 1 (n_1)	2	2	–
Number of DESCs in row 2 (n_2)	3	3	–
Flex. modulus of elasticity (E)	103	114	MPa
PolyFlex™ material tensile strength [62] (S_T)	29.0 ± 2.8	29.0 ± 2.8	MPa

Figure 13 shows a schematic of proof-of-concept prototypes of a spinal implant using a circular cross section (diameter = 92 mm) and an oval cross section. The oval cross section is the size of an invertebral disc, approximately an oval of 62 mm wide by 43 mm long. The oval DESC prototype was made by applying the DESC design to the CAD model from Ref. [63]. Flexures of 1 mm thickness were chosen as they do not exceed the tensile strength of the PolyFlex™ 3D-printing filament during stowing of the devices.

The values in Table 3 were used to calculate the force to stow the disc devices and their maximum stresses. Additionally, the parameters in Table 3 were used in the FEA and experimental models to validate the analytical models presented. Other parameters were also used to compare the presented equations for many different cases. The device will be actuated less than ten times so high cycle fatigue is not considered.

Figure 14 shows the proof-of-concept prototype spinal fusion implants with incorporated DESCs in the deployed and stowed positions. Table 4 lists the results calculated for the DESC devices. Note that because the devices are actuated from the center rigid section, the DESCs on either side of the center section require the same force. However, to actuate the central rod, the torque needed would be equal to 2F multiplied by the distance to the center of the shaft (d/2). When the physical prototypes compressed widths were measured, the widths for the circular and oval devices were approximately 46.0 and 27.8 mm, respectively. The differences in the measured and calculated values are largely due to the tolerances of the manufacturing processes and nonlinear material properties. Both physical prototypes, shown in Fig. 14, were made of PolyFlex™ 3D-printing filament (TPU95).

The results from Table 4 show that a device can be created that stows efficiently to allow for smaller incisions, while still being able to fill the desired deployed area. These results also show that the flexure parameters (width, thickness, length, initial curvature) can be adjusted to create a design with the desired stow force and stress that remains below the allowable stress to prevent failure. Additionally, the device presented here shows that the stored strain energy in the flexures can be used to help deploy the spinal fusion implant and provide some additional desired stiffening to the device.

Although the spinal fusion implant discussed here was the primary motivation for the development of DESCs, they could be used in other applications, including two noted below.

6.3 Linear Ratchet and Pawl. Figure 15 shows a linear ratchet mechanism with DESCs. The pawl in the mechanism was designed using DESCs, to attain the needed motion for ratcheting and was printed as a single piece. As the pawl is pushed through the rack, the DESCs compress flat, allowing the pawl to move to the next set of teeth. The DESCs expand back out to lock the device into the new position. The prototype was made of polylactic acid (PLA) with a flexural modulus of elasticity of 3.5 GPa. The length of the DESCs in the mechanism is 25.4 mm with an initial curvature of 0.041 mm^{-1} and thickness of 0.8 mm. The force needed to compress the DESCs on one side of the pawl is approximately 1.45 N/mm. As discussed earlier, a desired force can be

Downloaded from http://www.asmedigitalcollection.asme.org/mechanismsrobotics/article-pdf/14/2/021003/6759446/jmr_14_2_021003.pdf by guest on 03 November 2024

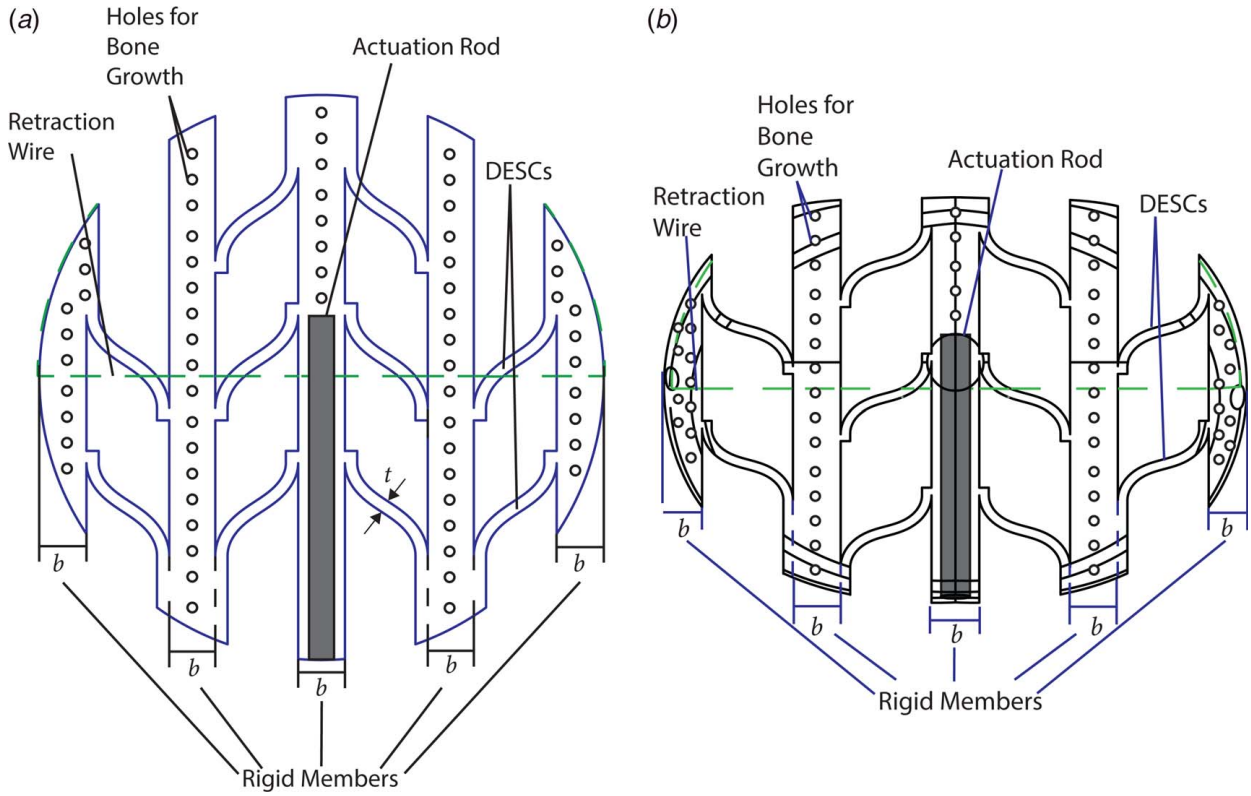

Fig. 13 Schematic of spinal implant device prototypes using DESCs. The dashed lines represent the retractor wires. (*a*) A schematic of the spine device using a circular cross-section. The gray box is the actuating rod used to stow the device. (*b*) A schematic of the spine device using an oval cross-section similar to an intervertebral spinal disc. The gray box connected to the hole at the bottom of the device is the actuation rod.

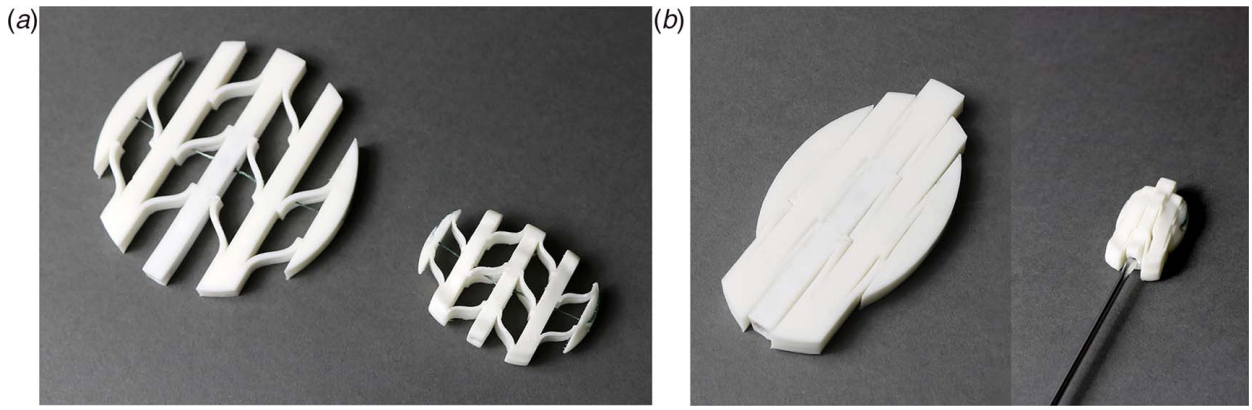

Fig. 14 Proof-of-concept spinal implant device prototypes using DESCs. The prototypes are made of PolyFlex™ filament (TPU95). (*a*) Physical prototypes of the circular and oval DESC spinal disc devices in their deployed states. The retractor wires can be seen running through the middle of both devices. (*b*) Physical prototypes of the circular and oval DESC spinal disc devices in their stowed states. The devices are retracted and held stowed by the wires being wound around the metal rod, in the center rigid segment.

Table 4 Calculated parameters of the DESC spinal devices

Configuration	Circular	Oval	Units
Calculated parameters			
Deployed area ($A_{top_{deployed}}$)	6648	2233	mm^2
Compressed width (W)	45.90	26.96	mm
Stowed area ($A_{front_{stowed}}$)	367.2	468.3	mm^2
Force to stow one side ($\overline{F}$)	3.16	1.39	N/mm
Maximum stress (σ_{max})	19.64	22.8	MPa

Downloaded from http://www.asmedigitalcollection.asme.org/mechanismsrobotics/article-pdf/14/2/021003/6759446/jmr_14_2_021003.pdf by guest on 03 November 2024

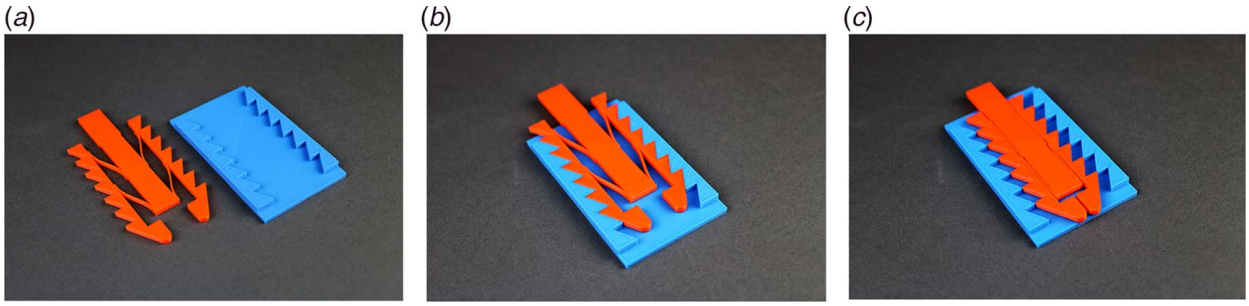

Fig. 15 Proof-of-concept DESC-enabled compact linear ratcheting mechanism. (*a*) Physical prototypes of a linear rachet mechanism using DESCs. (*b*) Physical prototypes of the pawl inserted into the rack. The DESCs compress minimally to fit into a set of teeth in the rack. (c) Physical prototypes of the pawl inserted into the rack. The DESCs will lay flat allowing the pawl to move into the next set of teeth.

determined by changing the initial curvature, length, or thickness of the DESCs or changing the material.

6.4 Other Possible Uses. Because the DESCs will lay flat when fully stowed and can be designed to lay flat at a specific force, they can be used to design mechanisms where the desired final position is flat. This gives the designer the ability to design the device for a specific desired force. Other applications of DESC flexures include use in mechanisms that absorb shock loads [64], such as in ski or snowboard bindings.

In its most general form, the DESC can be viewed as a fully compact spring which could have broad applications that extend well beyond the field of mechanism design.

7 Conclusions

This paper has applied the concept of the Euler spiral to design compliant connections that will lay flat when stowed, allowing compact stowing and the use of the stored strain energy for actuation. This is accomplished by solving the presented equations for the desired spans to determine the initial curvature, κ_0, and length, L, of the connections. Taylor Series approximations were used to solve for the desired variables to design the DESCs. Equations to determine the force-deflection behavior of these flexures and the maximum stress predicted were also presented. These equations show that the force and stress is dependent on (and can be tailored by changing) the flexure parameters. The results from these equations, FEA, and experimental data were compared and show good agreement.

A spinal disc implant was proposed as an application for DESCs. The forces needed to stow and accompanying stresses of two spinal devices were determined. These results showed that DESCs can be beneficial to the stowability and force-deflection design of these implants and show promise for other applications.

Acknowledgment

This paper is based on work supported by the National Science Foundation and the Air Force Office of Scientific Research through NSF Grant No. EFRI-ODISSEI-1240417, NSF Grant No. 1663345, and under the Air Force Office of Scientific Research Grant FA9550-19-1-0290 through Florida International University. Special thanks to Dr. Alden Yellowhorse for use of his code to compute the analytical solution to the Euler spiral, Brandon Sargent for the idea for the retraction method of the implant, Dr. Mohui Jin for the numerical method code used to solve the boundary value problem, and Pietro Bilancia for help with performing the FEA.

Conflict of Interest

There are no conflicts of interest.

Data Availability Statement

Data provided by a third party liste in Acknowledgment.

References

[1] Howell, L. L., 2001, *Compliant Mechanisms*, John Wiley & Sons, New York.
[2] Qiu, C., Aminzadeh, V., and Dai, J. S., 2013, "Kinematic Analysis and Stiffness Validation of Origami Cartons," ASME J. Mech. Des., **135**(11), p. 111004.
[3] DeFigueiredo, B., Pehrson, N. A., Tolman, K., Crampton, E., Magleby, S. P., and Howell, L. L., 2019, "Origami-Based Design of Conceal-and-Reveal Systems," ASME J. Mech. Rob., **11**(2), p. 020904.
[4] Hu, Y., Zhou, Y., and Liang, H., 2021, "Constructing Rigid-Foldable Generalized Miura-Ori Tessellations for Curved Surfaces," ASME J. Mech. Rob., **13**(1), p. 011017.
[5] Qiao, Q., Yuan, J., Shi, Y., Ning, X., and Wang, F., 2017, "Structure, Design, and Modeling of An Origami-Inspired Pneumatic Solar Tracking System for the NPU-Phonesat," ASME J. Mech. Rob., **9**(1), p. 011004.
[6] Xu, Y., Chen, L., Liu, W., Yao, J., Zhu, J., and Zhao, Y., 2018, "Type Synthesis of the Deployable Mechanisms for the Truss Antenna Using the Method of Adding Constraint Chains," ASME J. Mech. Rob., **10**(4), p. 041002.
[7] Pehrson, N. A., Ames, D. C., Smith, S. P., Magleby, S. P., and Arya, M., 2020, "Self-deployable, Self-Stiffening, and Retractable Origami-Based Arrays for Spacecraft," AIAA J., **58**(7), pp. 3221–3228.
[8] Maanasa, V., and Reddy, S. R. L., 2014, "Origami-Innovative Structural Forms and Applications in Disaster Management," Int. J. Curr. Eng. Technol., **4**(5), pp. 3431–3436.
[9] Deleo, A. A., O'Neil, J., Yasuda, H., Salviato, M., and Yang, J., 2020, "Origami-Based Deployable Structures Made of Carbon Fiber Reinforced Polymer Composites," Compos. Sci. Technol., **191**(11), p. 108060.
[10] Felton, S., Tolley, M., Demaine, E., Rus, D., and Wood, R., 2014, "A Method for Building Self-Folding Machines," Science, **345**(6197), pp. 644–646.
[11] Kalafat, M. A., Sevinç, H., Samankan, S., Altınkaynak, A., and Temel, Z., 2021, "A Novel Origami-Inspired Delta Mechanism With Flat Parallelogram Joints," ASME J. Mech. Rob., **13**(2), p. 021005.
[12] Edmondson, B., Bowen, L., Grames, C., Magleby, S., Howell, L., and Bateman, T., 2013, "Oriceps: Origami-Inspired Forceps," Proceedings of the ASME 2013 Conference on Smart Materials, Adaptive Structures and Intelligent Systems, Snowbird, UT, Sept. 16–18, SMASIS2013-3299.
[13] Xu, Y., Chen, Y., Liu, W., Ma, X., Yao, J., and Zhao, Y., 2020, "Degree of Freedom and Dynamic Analysis of the Multi-Loop Coupled Passive-Input Overconstrained Deployable Tetrahedral Mechanisms for Truss Antennas," ASME J. Mech. Rob., **12**(1), p. 011010.
[14] An, N., Li, M., and Zhou, J., 2020, "Modeling SMA-Enabled Soft Deployable Structures for Kirigami/Origami Reflectors," Int. J. Mech. Sci., **180**(9), p. 105753.
[15] Taylor, A., Miller, M., Fok, M., Nilsson, K., and Tse, Z. T. H., 2016, "Intracardiac Magnetic Resonance Imaging Catheter With Origami Deployable Mechanisms," ASME J. Med. Devices, **10**(2), p. 020957.
[16] Kuribayashi, K., Tsuchiya, K., You, Z., Tomus, D., Umemoto, M., Ito, T., and Sasaki, M., 2006, "Self-Deployable Origami Stent Grafts As a Biomedical Application of Ni-Rich Tini Shape Memory Alloy Foil," Mater. Sci. Eng. A, **419**(1–2), pp. 131–137.
[17] Sargent, B., Butler, J., Seymour, K., Bailey, D., Jensen, B., Magleby, S., and Howell, L., 2020, "An Origami-Based Medical Support System to Mitigate Flexible Shaft Buckling," ASME J. Mech. Rob., **12**(4), p. 041005.
[18] Ranzani, T., Russo, S., Schwab, F., Walsh, C. J., and Wood, R. J., 2017, "Deployable Stabilization Mechanisms for Endoscopic Procedures," 2017 IEEE International Conference on Robotics and Automation (ICRA), Singapore, May 29–June 3, IEEE, pp. 1125–1131.
[19] Gafford, J., Ding, Y., Harris, A., McKenna, T., Polygerinos, P., Holland, D., Walsh, C., and Moser, A., 2015, "Shape Deposition Manufacturing of a Soft, Atraumatic, and Deployable Surgical Grasper," ASME J. Mech. Rob., **7**(2), p. 021006.

Downloaded from http://www.asmedigitalcollection.asme.org/mechanismsrobotics/article-pdf/14/2/021003/6759446/jmr_14_2_021003.pdf by guest on 03 November 2024

[20] Bobbert, F., Janbaz, S., van Manen, T., Li, Y., and Zadpoor, A., 2020, "Russian Doll Deployable Meta-implants: Fusion of Kirigami, Origami, and Multi-Stability," Mater. Des., **191**, p. 108624.
[21] Baek, S.-M., Yim, S., Chae, S.-H., Lee, D.-Y., and Cho, K.-J., 2020, "Ladybird Beetle-Inspired Compliant Origami," Sci. Rob., **5**(41), p. eaaz6262.
[22] Seymour, K., Burrow, D., Avila, A., Bateman, T., Morgan, D. C., Magleby, S. P., and Howell, L. L., 2018, "Origami-based Deployable Ballistic Barrier," Proceedings of the 7th International Meeting on Origami in Science, Mathematics and Education, Oxford, UK, Sept. 4–7.
[23] Tolman, K. A., Crampton, E. B., Stucki, C., Maynes, D., and Howell, L. L., 2018, "Design of An Origami-Inspired Deployable Aerodynamic Locomotive Fairing," Proceedings of the 7th International Meeting on Origami in Science, Mathematics, and Education, UK, Sept. 4–7.
[24] Chen, B., Hu, J., Chen, W., and Qi, J., 2020, "Geometrical Analysis of Connecting Beam Mandala: A Planar Deployable Mechanism," ASME J. Mech. Rob., **12**(1), p. 011009.
[25] Banerjee, H., Pusalkar, N., and Ren, H., 2018, "Single-Motor Controlled Tendon-Driven Peristaltic Soft Origami Robot," ASME J. Mech. Rob., **10**(6), p. 064501.
[26] Guang, C., and Yang, Y., 2018, "Single-vertex Multicrease Rigid Origami With Nonzero Thickness and Its Transformation Into Deployable Mechanisms," ASME J. Mech. Rob., **10**(1), p. 011010.
[27] Badagavi, P., Pai, V., and Chinta, A., 2017, "Use of Origami in Space Science and Various Other Fields of Science," Second IEEE International Conference on Recent Trends in Electronics, Information Communication Technology (RTEICT), Bangalore, India, May 19–20, pp. 628–632.
[28] Morgan, J., Magleby, S. P., and Howell, L. L., 2016, "An Approach to Designing Origami-Adapted Aerospace Mechanisms," ASME J. Mech. Des., **138**(5), p. 052301.
[29] Thrall, A., and Quaglia, C., 2014, "Accordion Shelters: A Historical Review of Origami-Like Deployable Shelters Developed by the US Military," Eng. Struct., **59**, pp. 686–692.
[30] Peraza-Hernandez, E. A., Hartl, D. J., Malak Jr, R. J., and Lagoudas, D. C., 2014, "Origami-Inspired Active Structures: A Synthesis and Review," Smart Mater. Struct., **23**(9), p. 094001.
[31] Banerjee, H., Li, T. K., Ponraj, G., Kirthika, S. K., Lim, C. M., and Ren, H., 2020, "Origami-Layer-Jamming Deployable Surgical Retractor With Variable Stiffness and Tactile Sensing," ASME J. Mech. Rob., **12**(3), p. 031010.
[32] Zhao, N., and Harne, R. L., 2021, "Reconfigurable Acoustic Arrays With Deployable Structure Based on a Hoberman–miura System Synthesis," ASME J. Mech. Des., **143**(6), p. 063301.
[33] Zhuo, S., Zhang, G., Feng, X., Jiang, H., Shi, J., Liu, H., and Li, H., 2016, "Multiple Shape Memory Polymers for Self-Deployable Device," RSC Adv., **6**(56), pp. 50581–50586.
[34] Song, X., Guo, H., Chen, J., Yuan, W., and Xu, Y., 2021, "Double-Layer Deployable Mechanical Network Constructed of Threefold-Symmetric Bricard Linkages and Sarrus Linkages," ASME J. Mech. Rob., **13**(6), p. 061010.
[35] Wang, J., and Kong, X., 2018, "A Novel Method for Constructing Multi-Mode Deployable Polyhedron Mechanisms Using Symmetric Spatial RRR Compositional Units," International Design Engineering Technical Conferences and Computers and Information in Engineering Conference, Quebec City, Canada, Aug. 26.
[36] Yang, F., You, Z., and Chen, Y., 2020, "Foldable Hexagonal Structures Based on the Threefold-Symmetric Bricard Linkage," ASME J. Mech. Rob., **12**(1), pp. 011012.
[37] Alfattani, R., and Lusk, C., 2020, "Shape-Morphing Using Bistable Triangles With Dwell-Enhanced Stability," ASME J. Mech. Rob., **12**(5), p. 051003.
[38] Yang, F., Gao, Y., Lu, S., and Chen, K., 2021, "A Mobile Bennett Network Constructed With Identical Square Panels," ASME J. Mech. Des., **143**(11), p. 113301.
[39] Suthar, B., and Jung, S., 2021, "Design and Bending Analysis of a Metamorphic Parallel Twisted-Scissor Mechanism," ASME J. Mech. Rob., **13**(4), p. 040905.
[40] Nelson, T. G., Zimmerman, T. K., Magleby, S. P., Lang, R. J., and Howell, L. L., 2019, "Developable Mechanisms on Developable Surfaces," Sci. Rob., **4**(27), pp. eaau5171.
[41] Puig, L., Barton, A., and Rando, N., 2010, "A Review on Large Deployable Structures for Astrophysics Missions," Acta Astronautica, **67**(1–2), pp. 12–26.
[42] Zhao, J.-S., Chu, F., and Feng, Z.-J., 2009, "The Mechanism Theory and Application of Deployable Structures Based on SLE," Mech. Mach. Theory, **44**(2), pp. 324–335.
[43] Langbecker, T., 1999, "Kinematic Analysis of Deployable Scissor Structures," Int. J. Space Struct., **14**(1), pp. 1–15.
[44] Nelson, T. G., Baldelomar Pinto, L. M., Bruton, J. T., Deng, Z., Nelson, C. G., and Howell, L. L., 2021, "Deployable Convex Generalized Cylindrical Surfaces Using Torsional Joints," ASME J. Mech. Rob., **13**(3), p. 031003.
[45] She, Y., Gu, Z., Song, S., Su, H.-J., and Wang, J., 2021, "Design, Modeling, and Manufacturing of a Variable Lateral Stiffness Arm Via Shape Morphing Mechanisms," ASME J. Mech. Rob., **13**(3), p. 031020.
[46] Qaiser, Z., and Johnson, S., 2021, "Generalized Spiral Spring: A Bioinspired Tunable Stiffness Mechanism for Linear Response With High Resolution," ASME J. Mech. Rob., **13**(1), p. 011007.
[47] Levien, R. L., 2009, "From Spiral to Spline: Optimal Techniques in Interactive Curve Design," Ph.D. thesis, EECS Department, University of California, Berkeley, CA.
[48] Yellowhorse, A., and Howell, L. L., 2018, "Deployable Lenticular Stiffeners for Origami-Inspired Mechanisms," Mech. Des. Struct. Mach., **46**(5), pp. 634–649.
[49] Alhajyaseen, W. K., Asano, M., Nakamura, H., and Tan, D. M., 2013, "Stochastic Approach for Modeling the Effects of Intersection Geometry on Turning Vehicle Paths," Transportation Res. Part C: Emerging Technol., **32**, pp. 179–192.
[50] Marzbani, H., Jazar, R. N., and Fard, M., 2015, "Better Road Design Using Clothoids," Sustainable Automotive Technologies 2014, Proceedings of the 6th ICSAT, I. Denbratt, A. Subic, and J. Wellnitz, eds., Springer, Cham, Switzerland, pp. 25–40.
[51] Kimia, B. B., Frankel, I., and Popescu, A. -M., 2003, "Euler Spiral for Shape Completion," Int. J. Comput. Vision, **54**(1), pp. 159–182.
[52] Harary, G., and Tal, A., 2012, "3d Euler Spirals for 3D Curve Completion," Comput. Geometry, **45**(3), pp. 115–126.
[53] ASTM International, 2017, *Standard Test Methods for Flexural Properties of Unreinforced and Reinforced Plastics and Electrical Insulating Materials*, ASTM International, West Conshohocken, PA, Standard ASTM D790-17.
[54] McDermott, K. W. I. W. H., Freeman, W. J. A., and Elixhauser, A. A., 2017, Overview of Operating Room Procedures During Inpatient Stays in U.S. Hospitals, 2014. HCUP Statistical Brief #233. Agency for Healthcare Research and Quality, Rockville, MD. On the WWW, December. www.hcup-us.ahrq.gov/reports/statbriefs/sb233-Operating-Room-Procedures-United-States-2014.pdf
[55] Rajaee, S. S., Bae, H. W., Kanim, L. E., and Delamarter, R. B., 2012, "Spinal Fusion in the United States: Analysis of Trends From 1998 to 2008," Spine, **37**(1), pp. 67–76.
[56] Peck, J. H., Kavlock, K. D., Showalter, B. L., Ferrell, B. M., Peck, D. G., and Dmitriev, A. E., 2018, "Mechanical Performance of Lumbar Intervertebral Body Fusion Devices: An Analysis of Data Submitted to the Food and Drug Administration," J. Biomech., **78**, pp. 87–93.
[57] Goz, V., Weinreb, J. H., Schwab, F., Lafage, V., and Errico, T. J., 2014, "Comparison of Complications, Costs, and Length of Stay of Three Different Lumbar Interbody Fusion Techniques: An Analysis of the Nationwide Inpatient Sample Database," Spine J., **14**(9), pp. 2019–2027.
[58] Ozgur, B. M., Aryan, H. E., Pimenta, L., and Taylor, W. R., 2006, "Extreme Lateral Interbody Fusion (xlif): a Novel Surgical Technique for Anterior Lumbar Interbody Fusion," Spine J., **6**(4), pp. 435–443.
[59] Kao, T.-H., Wu, C.-H., Chou, Y.-C., Chen, H.-T., Chen, W.-H., and Tsou, H.-K., 2014, "Risk Factors for Subsidence in Anterior Cervical Fusion With Stand-Alone Polyetheretherketone (peek) Cages: A Review of 82 Cases and 182 Levels," Arch. Orthop. Trauma Surg., **134**(10), pp. 1343–1351.
[60] Halverson, P. A., Bowden, A. E., and Howell, L. L., 2012, "A Compliant-Mechanism Approach to Achieving Specific Quality of Motion in a Lumbar Total Disc Replacement," Int. J. Spine Surg., **6**(1), pp. 78–86.
[61] Dodgen, E., Stratton, E., Bowden, A., and Howell, L., 2012, "Spinal Implant Development, Modeling, and Testing to Achieve Customizable and Nonlinear Stiffness," ASME J. Med. Devices, **6**(2), p. 021010.
[62] Polymaker, 2018, *PolyFlex™ TPU95 Technical Data Sheet*, Nov. 2018. Version 4.0.
[63] Masni-Azian, , and Tanaka, M., 2017, "Statistical Factorial Analysis Approach for Parameter Calibration on Material Nonlinearity of Intervertebral Disc Finite Element Model," Comput. Methods Biomech. Biomed. Eng., **20**(10), pp. 1066–1076.
[64] Tolman, S. S., Delimont, I. L., Howell, L. L., and Fullwood, D. T., 2014, "Material Selection for Elastic Energy Absorption in Origami-Inspired Compliant Corrugations," Smart Mater. Struct., **23**(9), p. 094010.

Downloaded from http://www.asmedigitalcollection.asme.org/mechanismsrobotics/article-pdf/14/2/021003/6759446/jmr_14_2_021003.pdf by guest on 03 November 2024